

## RESEARCH ARTICLE

# Fault-Tolerant Dual Channels Three-Phase PMSM for Aerospace Applications

MUHAMMAD RAZA KHOWJA<sup>1</sup>, KULDEEP SINGH<sup>1</sup>, ANTONINO LA ROCCA<sup>1</sup>, GAURANG VAKIL<sup>1</sup>, (Member, IEEE), RAMKUMAR RAMNATHAN<sup>1</sup>, AND CHRIS GERADA<sup>1,2</sup>, (Member, IEEE)

<sup>1</sup>PEMC Research Group, University of Nottingham, NG7 2GT Nottingham, U.K.

<sup>2</sup>Key Laboratory of More Electric Aircraft Technology of Zhejiang Province, Ningbo 315100, China

Corresponding author: Muhammad Raza Khowja (Raza.Khowja@nottingham.ac.uk)

**ABSTRACT** In safety-critical applications such as aerospace and marine, electrical machines are limited to meet several stringent requirements such as physical, electrical, magnetic and thermal isolation between two three-phase channels, in order to be considered for fault-tolerant operation throughout its service life. This paper presents novel sectorized fault-tolerant PM synchronous machines which include single, double and four sectorized designs where one pole pair section of the machine's stator is cut out to meet the fault-tolerant constraints. A detailed electromagnetic analysis is carried out in terms of their electromagnetic performance which is then compared with the benchmark 30s/10p combination for a given output power of 50kW. Due to the heightened power density in the innovative design, a highly effective thermal management system became necessary. This led to the identification of a novel and efficient cooling configuration. Leveraging the four gaps between the four sectors, an efficient cooling system was successfully implemented. As a result, the current density increased by 18.2%, representing an increase of 2A/mm<sup>2</sup> compared to the benchmark machine design.

**INDEX TERMS** Dual three-phase PMSM, fault-tolerant machine, finite element model, numerical methodology, computational fluid dynamics and aerospace applications.

## I. INTRODUCTION

Fault-tolerant multiphase machines allow the aerospace industry to use it for safety-critical applications due to its potential benefits such as high power density, high efficiency, reliability, and redundancy when compared to standard three-phase PM synchronous machines [1]. Most importantly, physical, magnetic, thermal and electrical isolation can be achieved with specific slot/pole combination which gives the zero mutual coupling effect between the three-phase channels [2], [3]. The slot/pole combinations for fault-tolerant motors only deal with the concentrated stator windings [2] which eliminate distributed windings away from selecting the fault-tolerant motors, despite of its highest winding factor.

Multi-phase fault-tolerant machines can be wound with symmetrical three-phase windings where the winding is

phase-shifted by a fixed angle from other phases which allows simple control of the air-gap magnetic field [4]. The fault-tolerant machine can be segmented either with axial or radial segments on the stator periphery which must deliver magnetic, electrical and physical isolation between the phases of the other three-phase units [5].

In [2] and [5], the radial and axial segmentation are used to increase the reliability and safety of the helicopter actuation system. In radial segmentation, two three-phase channels are separately wound in different stator sectors to achieve higher electromagnetic isolation whereas two identical separate machines are mounted on the shaft axis in axial segmentation. The benefits of radial segmentation are short end-winding overhang and a smaller number of components required. However, it requires a higher converter rating due to heavy rotor inertia and high acceleration torque. On the other hand, axial segmentation essentially offers magnetic and thermal independence but requires a significant amount

The associate editor coordinating the review of this manuscript and approving it for publication was Alfeu J. Sguarezi Filho<sup>1</sup>.

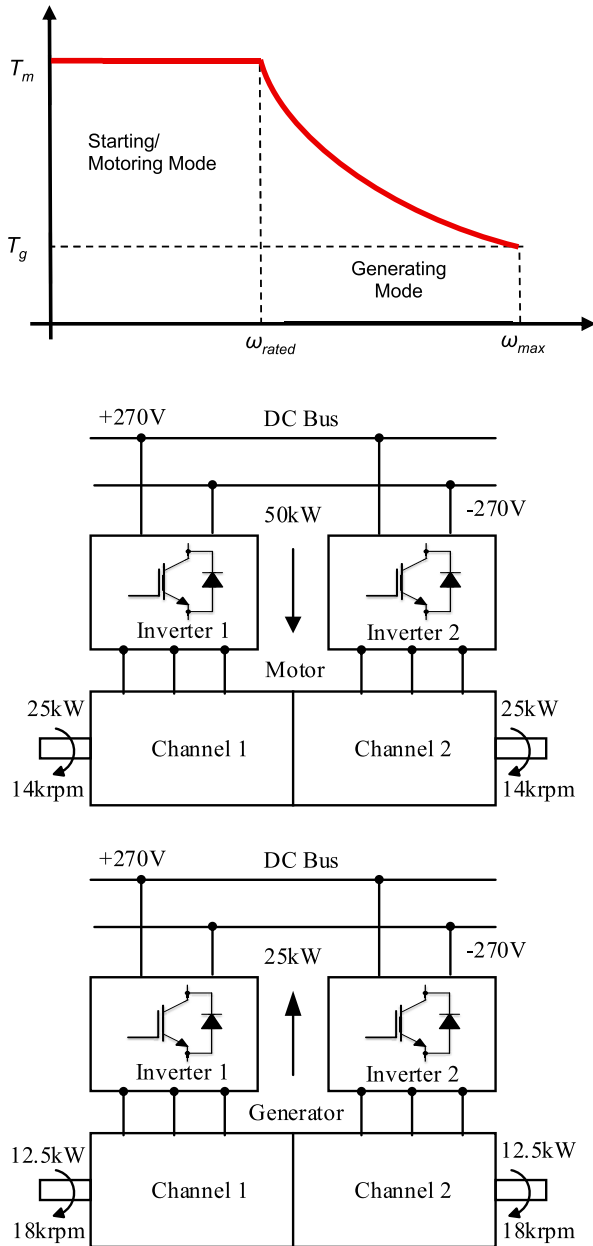


**FIGURE 1.** Application requirements (a) torque-speed characteristics (b) Fault-tolerant system operating in motoring mode (c) Fault-tolerant system operating in generating mode.

of volume due to extra space occupied by the end-windings overhang [5]. A new multi three-phase SMPM synchronous machine is investigated with triple three-phase arranged in three sectors of the stator, fed by three separate voltage source inverters. Three sectors are created by introducing air or iron between each three-phase unit. However, the drawback of such machines is that it reduces the slot area to create the space for segmentation which increases the complexity in control and current density of a conductor resulting in temperature increase [1]. In [6] investigated thermal management of two fault-tolerant permanent magnet synchronous machines (PMSMs) designed for aerospace applications. In this study,

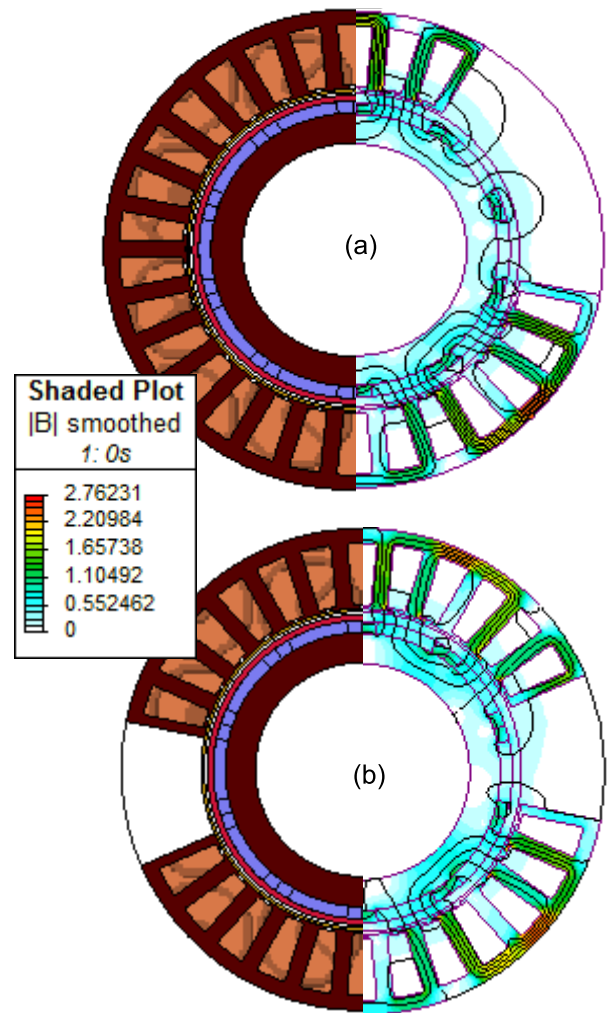


**FIGURE 2.** Radial cross-section and flux distribution of Sected PM Machines (a) Single sector PM synchronous machine (b) Double sectors PM synchronous machine.

simplified thermal models based on lumped parameter thermal network (LPTN) were used. Without the fine-tuning process, it would be difficult to determine the LPTN's critical parameters such as convective heat transfer coefficient and equivalent slot conductivity. Article [7] investigated direct and indirect cooling using LPTN. Oil cooled traction drive is considered for the direct cooling. The study also examined fluid aging under high temperatures, finding minimal changes in fluid properties, indicating stable long-term performance. In [8] highlighted the importance of advanced thermal management methods for electric vehicle (EV) motors, focusing on the oil spray cooling approach. This study showed that spray cooling is an effective way to cool end-winding. The optimum selection of parameters such as spray patterns, spray coverage, flow rate, and droplet size is crucial in an efficient cooling system. The studies such as [9], [10], [11], and [12] highlighted the requirements of an efficient cooling system to extract heat from a power dense machine. Some more previous works on the machine's stator segmentation have been

**TABLE 1.** Specifications of benchmark or existing machine.

PARAMETERS	VALUE	UNIT
Slot/Pole Number	30/10	-
Iron Material	Cobalt Iron	-
PM Material	Recoma 33E	-
DC-Link Voltage per channel	540 ( $\pm 270V$ )	V
Number of Turns per coil	16	-
Active Stack Length	60	mm
Estimated End-windings overhang	2 $\times$ 12.5	mm
Base and Max. Speed	14 and 18	kRPM
Output Torque at 14krpm & 18krpm	35 & 13.5	Nm
Output Power at 14krpm & 18krpm	50 & 25	kW
Housing Diameter	170	mm
Stator Outer & Bore Diameter	160 & 107	mm
Slot Fill Factor	0.5	-
Shaft Diameter	90	mm
PM Thickness	4.0	mm
Stator & Rotor Sleeves	1 & 2	mm
Airgap	2.0	mm

**TABLE 2.** Possible combinations for double sectored machine.

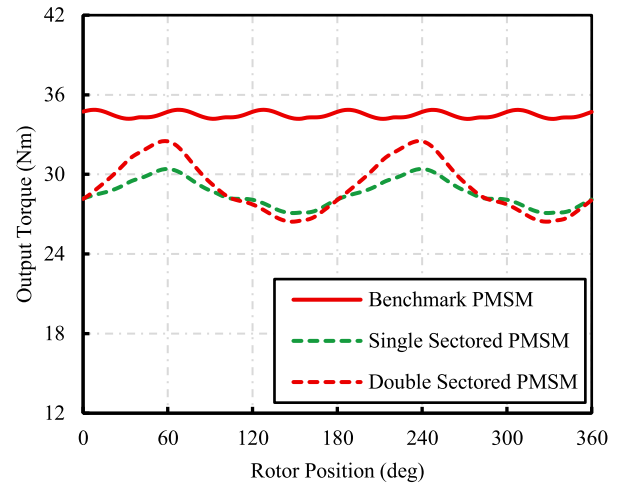
ACTUAL SLOT-POLE COMBINATION	SLOTS LEFT PER CHANNEL
18s/6p	6
30s/10p	12
42s/14p	18
54s/18p	24

carried out for manufacturing issues [13], [14] or improving the machine's performance [15], [16]. In this paper, new designs of dual three-phase PM synchronous machines are proposed to meet the fault-tolerant requirements. The proposed concept removes the one pole pair section from the stator that allows the machine to operate independently in terms of electrical, mechanical, thermal and magnetic isolation between the three-phase units. In section II, motor drive requirements are presented including torque-speed characteristics, coolant and envelope limitations and fault-tolerant needs. Section III introduces an idea of the sectored three-phase PM synchronous machine with its pros and cons detailed, finite element modeling, torque behavior and unbalanced radial forces. Section IV describes the thermal analyses carried out to investigate the thermal performance of the proposed machine design. Section V describes the numerical (CFD) methodology followed to achieve an optimized cooling approach capable of maximizing the power density and the overall efficiency. Section VI presents the validation of the present numerical methodology. Section VII highlights the key results obtained from the thermal analysis and the paper is concluded in section VIII.

## II. APPLICATION REQUIREMENTS

### A. TORQUE-SPEED REQUIREMENTS

The electrical machine must be designed to meet the torque-speed requirements as depicted in Figure. 1a. The

**FIGURE 3.** Full-load torque comparison of benchmark machine and novel sectored machines.

fault-tolerant system in both starter and generator modes are illustrated in Figure 1b and Figure 1c respectively. The machine feeds into a 540V ( $\pm 270V$ ) DC bus, which must deliver at least 50 kW or more during starting or motoring mode and 25kW at 18 kRPM in generation mode. During the engine-starting period, the machine operates as a motor and is required to deliver constant torque from standstill to the rated speed. In motoring mode, it must produce a minimum output power of 50 kW. Once the engine is started, the machine transitions to generation mode, supplying at least 25 kW of power at 18 kRPM to the aircraft system's electrical distribution network.

### B. FAULT-TOLERANCE REQUIREMENT

The machine must feature dual three-phase channels to enhance the system's reliability and safety. Each channel is required to deliver at least 25 kW at 14 kRPM and 12.5 kW mechanical power at 18 kRPM, both connected to a common 540V DC-link bus. The fault-tolerant design considerations include [6], [17]:

- Physical Separation of Phases:** The winding arrangement must ensure that each three-phase unit has physically separated phases to prevent cross-phase faults.
- Thermal and Magnetic Decoupling:** Each three-phase unit must be thermally and magnetically decoupled to avoid mutual coupling effects, which can interfere with fault isolation and machine performance.
- Independent Electrical Connections:** The electrical connections of each unit are brought out of the machine, allowing them to power the aircraft's load independently, enhancing redundancy and fault isolation.

The fault-tolerant design impacts the torque-speed requirements by necessitating certain trade-offs:

TABLE 3. Performance comparison of benchmark & novel sectored machines.

MACHINE DESIGN	TORQUE RIPPLE	MAGNETIC DECOUPLING	PHYSICAL ISOLATION	THERMAL DECOUPLING	RADIAL FORCES
Benchmark Machine (30s10p)	++	×	--	×	++
Single Sectored PMSM	-	--	--	×	--
Double Sectored PMSM	--	++	++	+	++
Four Sectored PMSM	+	++	++	+	++

++ Best    + Good    - Bad    -- Worst    × Not Possible

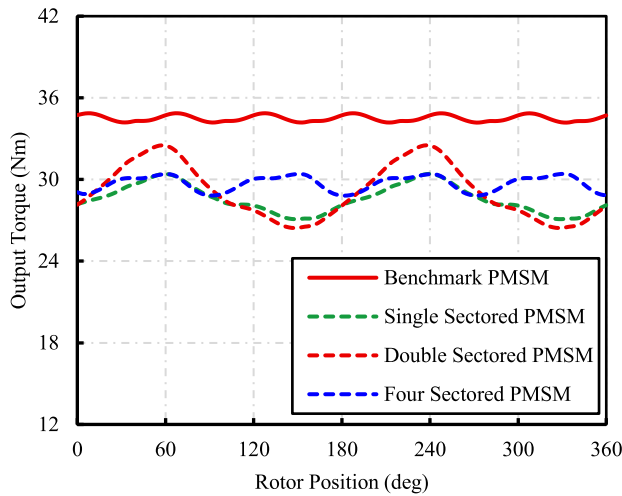


FIGURE 4. Full-load torque comparison of benchmark machine and novel sectored machines.

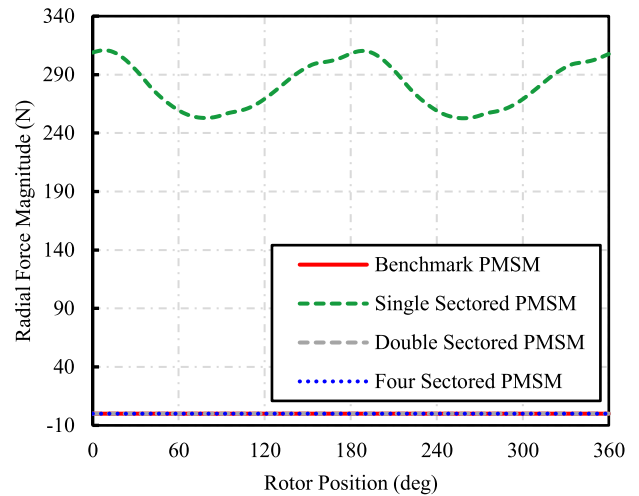


FIGURE 5. Comparison of stator and rotor radial forces of sectored PM synchronous machines.

- a. **Physical Separation and Decoupling:** Ensuring physical separation and decoupling can lead to increased machine size and reduced power density. For example, a radially segmented single layer 12s/10p configuration can meet all fault-tolerant requirements but results in lower power density and higher end-windings overhang compared to a double layer 18s/12p configuration [5].
- b. **Independent Channels:** The dual-channel design means each channel must be capable of meeting a portion of the total power requirement independently.
- c. In the event of a fault, the machine must still deliver sufficient torque and speed performance within the operational limits. This redundancy ensures that the machine can maintain operation without complete shut-down, but it also requires more robust design and can affect overall efficiency.

Therefore, while the machine can meet both the torque-speed and fault-tolerance requirements, achieving a balance between these can lead to design compromises. A configuration that meets all fault-tolerance requirements may sacrifice power density and require a larger space envelope, impacting the overall system design and efficiency.

**C. COOLANT AND SPACE LIMITATIONS**

The maximum allowable winding temperature is limited to 180°C. Engine oil is available as a coolant and can be

circulated through the stator slots at a flow rate of 5 l/min. The properties of cooling oil are summarized in Table 6. On the other hand, the total volume available to accommodate the electrical machine, power electronics, and control boards is restricted to dimensions of 175 mm outer diameter, 90 mm inner diameter, and 150 mm axial length.

**III. NOVEL SECTORED PM MACHINE**

To enhance the fault-tolerance capabilities, this section investigates novel sectored permanent magnet (PM) synchronous machines, including:

- Single sectored PM machine
- Double sectored PM machine
- Four sectored PM machine (introduced later)

These sectors are created by removing one pole pair section of the winding (i.e., 6 slots) from the stator while maintaining the same number of poles on the rotor, as depicted in Figure 2a and Figure 2b. For this application, a conventional 30 slots/10 poles (30s/10p) distributed wound machine is considered and modified to improve its fault-tolerance. Detailed specifications of benchmark machine are shown in Table 1.

**A. POSSIBLE COMBINATIONS**

There is no limitation on selecting a slot-pole combination for a single sectored PM synchronous machine. However, for a double sectored PM synchronous machine, the slot-pole

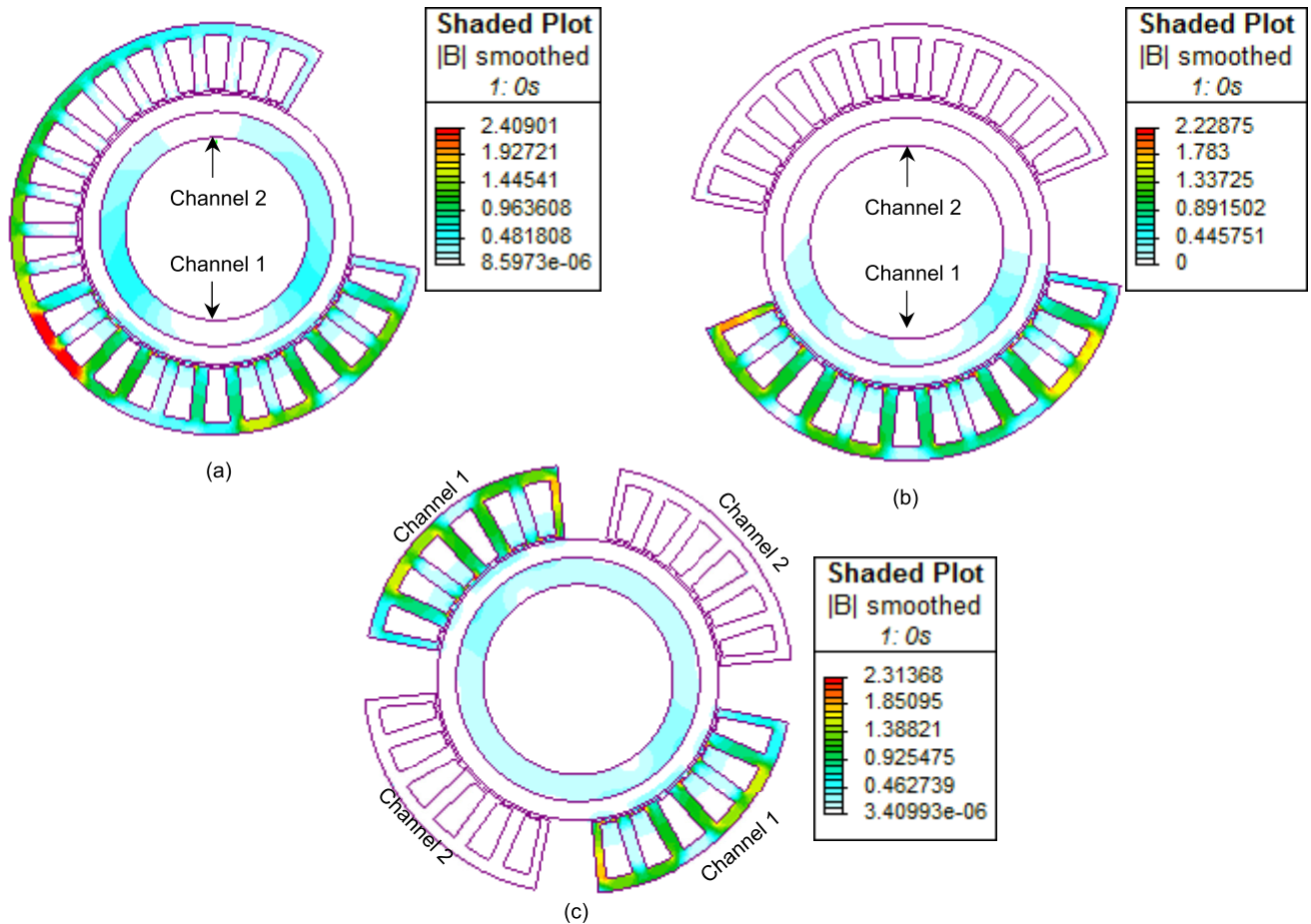


**FIGURE 6.** Magnetic Decoupling of Sectored PMSM (a) Single Sectored Machine (b) Double Sectored Machine (c) Four Sectored Machine.

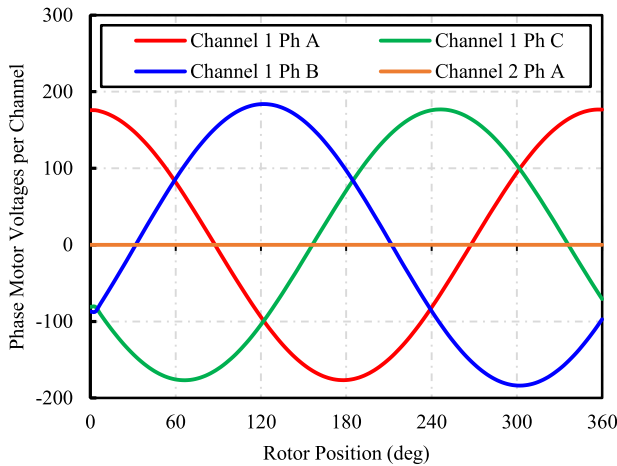


**FIGURE 7.** Three-phase Motor Voltages of Double and four sectored Synchronous Machine when one channel is open-circuited.

combination must be selected such that each section (or channel) of the machine remains a multiple of 6 slots, to form a distributed winding. Table 2 shows the possible combinations for the double sectored machine. It can be observed that the 30s/10p configuration, which provides 12 slots for each three-phase channel, has been selected for further investigation. In contrast, the 42s/14p combination is avoided due to its high

fundamental frequency and the challenges associated with the lamination manufacturing process of its stator. Additionally, the 18s/6p configuration is discarded due to its low number of poles, which would result in low power density.

**B. FINITE ELEMENT (FE) MODEL**

The finite element [18] models for the existing machine, single, double, and four-sectioned machines were built using the commercial software “MagNet” by Infolytica. The non-linear convergence method (Newton-Raphson) was used with a maximum of 50 iterations and a polynomial order of 2. The Newton tolerance was 0.1% and the CG tolerance was 0.01%. The mesh element size was 1mm for the stator and rotor, while the air gap had a mesh element size of 0.5mm. One pole pair section was removed from the benchmark or existing machine (30s/10p), the parameters of which are detailed in Table 1. The radial cross-section and flux distribution for the single and double sectored PM machines are depicted in Figure 2a and Figure 2b, respectively. From Figure 2, it is clearly evident that the leakage flux, originating from where the sectors are created, results in higher torque ripple. This is also illustrated in Figure 3 where the torque of each machine is presented and compared against the benchmark machine. It should be noted that the output torque

**TABLE 4.** Loss comparison of benchmark & novel sectored machines.

Parameters	Benchmark Machine	Single Sectored Machine	Double Sectored Machine	Four Sectored Machine
RMS Current	57.6 A	68.1 A	68.1 A	68.1 A
RMS Current Density	11 A/mm <sup>2</sup>	13 A/mm <sup>2</sup>	13 A/mm <sup>2</sup>	13 A/mm <sup>2</sup>
Stator Iron Loss	0.249 kW	0.286 kW	0.306 kW	0.351 kW
Copper Loss	1.868 kW	2.168 kW	2.68 kW	2.168 kW

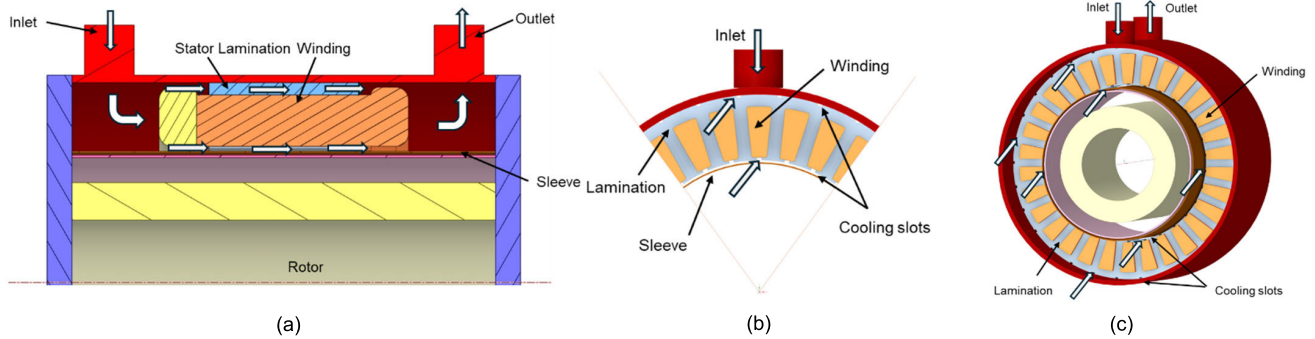


**FIGURE 8.** Schematic of Cooling Configuration (a) 2D Axial view (b) 2D Radial view (c) 3D view.

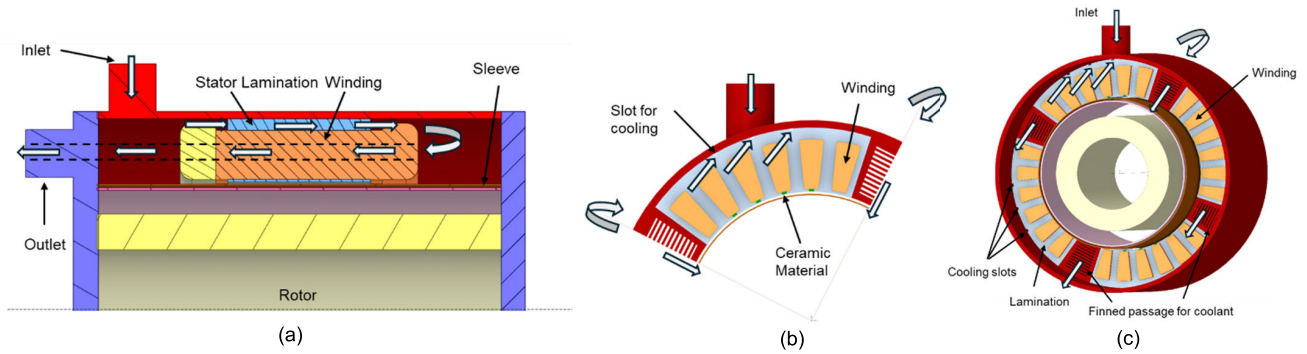


**FIGURE 9.** Schematic of updated Cooling Configuration (a) 2D Axial view (b) 2D Radial view for four sectored PM Machine (c) 3D view.

is expected to decrease to approximately one-fifth of the benchmark machine’s torque due to the removal of one pole pair winding section from the stator. The comparison of the average torque and its associated torque ripple for all three machine designs is illustrated in Table 3. The mean torque of the single and double sectored PM machines are 28.6 Nm and 29 Nm respectively, compared to 35 Nm for the benchmark machines. The percentage torque ripple for the single and double sectored machine designs are 11.6% and 20.9% respectively, significantly higher than the 2% observed in the benchmark machine. This torque ripple can be improved either by 1) applying different control methods or by 2) modifying the machine’s physical layout. By applying the carrier phase shift (CPS-PWM) control method it is possible to reduce the machine’s torque ripple to a considerable amount. In [12], the author has claimed that the peak-to-peak values of the torque waveforms obtained by applying CPS-PWM are reduced by 63.8% and 53.3% when compared with the traditional control system in FEA and experimental results respectively.

To reduce the torque ripple from a design perspective, the double sectored PM synchronous machine has been further

divided into four sectors instead of two, as shown in Figure 4. As illustrated, each sector of the four sectored PM machine is physically separated by 90 degrees. Consequently, it can be supplied by two inverters, each supplying two sectors that are 180 degrees apart, making it a viable option for a fault-tolerant motor drive system. The torque ripple of the four sectored PM machine, alongside those of the benchmark PM machine, the single sectored, and double sectored PM synchronous machines, can be observed in Figure 5. As expected, the torque ripple in the four sectored PM machine has been considerably reduced to 5.2%, which is comparable with the 2% torque ripple of the benchmark machine with no sectors.

**C. RADIAL FORNCES ON THE STATOR AND ROTOR**

The radial forces exerted on the stator can significantly stress the rotor bearings and may lead to radial vibrations, potentially causing undesired noises. Therefore, it is important to examine the radial forces acting on the rotor under normal operating conditions. Figure 5 compares the radial forces on the stator and rotor when both three-phase channels are

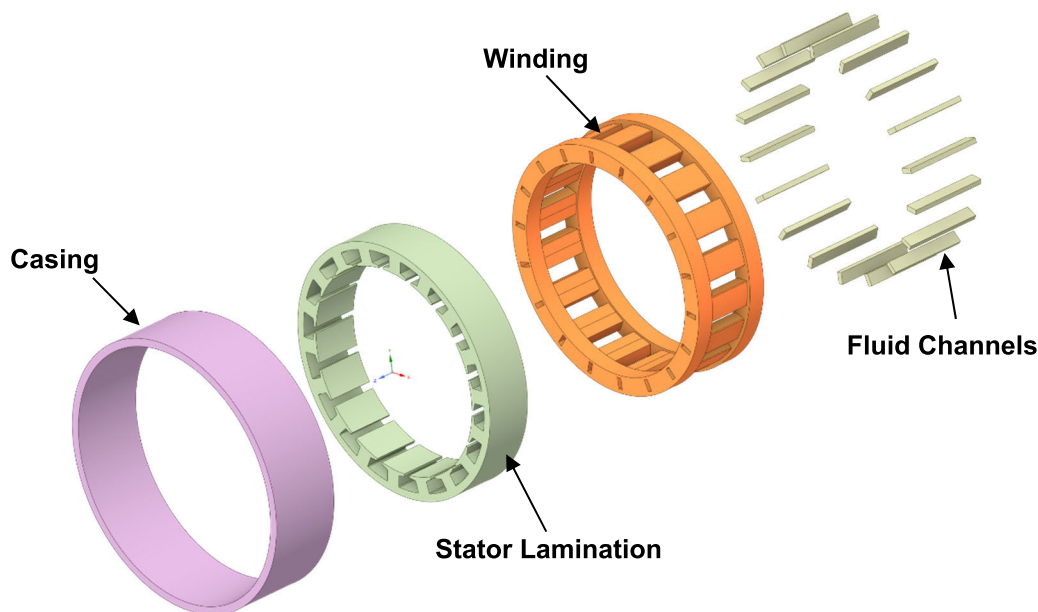


**FIGURE 10.** Exploded view of the benchmark machine used to validate the numerical methodology.

fully operational and fed by the current source at rated current. As expected, the single sectored PM machine generates higher radial forces due to its asymmetrical physical structure, leading to an unbalanced radial force on both the stator and rotor. In contrast, the unbalanced radial forces on the stator and rotor are negligible in the case of the double and four sectored PM synchronous machines, due to its symmetrical structure.

#### D. MAGNETIC COUPLING

This section investigates the effect of magnetic coupling. The permanent magnets were disabled from the FE model and the stator of channel 1 was supplied at rated current and speed, whereas channel 2 was fed with no currents. Figure 6 shows the results of the magnetic coupling between the channels for the single, double, and four sectored PM machines, respectively. Magnetic isolation is achieved by creating air segmentations between the channels. When one channel operates under normal conditions and another is open-circuited, no flux linkage is observed in the double and four sectored PM machines, as shown in Figure 6b and Figure 6c. The 3-phase motor voltages between two channels for the double and four sectored PM machines are plotted in Figure 7.

#### IV. THERMAL EVALUATION

These motor voltage waveforms confirm that the magnetic interaction between the two channels is negligible, thereby making these configurations ideal candidates for fault-tolerant motor drives. Due to their low torque ripple, the double and four sectored PM machines have been selected for thermal analysis. To ensure a fair comparison, the full load current of all sectored machines is adjusted to produce the same output power (50kW) as the benchmark machine (30s/10p). Accordingly, the full-load RMS current is adjusted

from 57.6 A to 68.1 A. The corresponding stator iron and copper losses are illustrated in Table 4.

Detailed conjugate thermal analyses were carried out to assess the thermal behaviour of the original design and the four-sector design; indeed, the latter is expected to provide the best performance among the three alternative designs. The thermal management is carried out according to the following two design criteria:

- The cooling configurations adopted to be fully included within the volume available and
- The thermal performance of the four-sector design equalizes or exceeds the benchmark design.

Due to the high-power density required a direct cooling arrangement was preferred; this consists in a semi-flooded configuration where the coolant flows through the stationary part only, whilst the rotor region is fully enclosed by using a stator sleeve inserted into the stator bore. Given the high-speed of the application, such solution helps maintaining the level of windage loss acceptable whilst still achieving an intensive cooling effect. A comparison of cooling configurations of the baseline motor and four-sectored machine is shown in Figure 8 and Figure 9 respectively. Figure 8a shows the front view of the cooling configuration of the baseline machine. Cooling oil enters from the driving end into the space between the endplates and stator sleeve which eventually flows through the cooling slots as shown in Figure 8b. The cooling oil after extracting heat from the end-windings, stator lamination and active part of the windings exist from the non-driving end as depicted in Figure 8a and Figure 8c respectively. Indeed, several studies available in literature have shown the significant benefit of using direct cooling options for maximising the performance [19], [20], [21], [22], [23], [24], [25], [26]. Significantly higher operating

temperatures can be expected in the sectored machines due to higher power density. An alternative cooling approach aimed at taking advantage of the gaps available between the sectors was considered for one, two and four-sectored machines. Due to brevity, the cooling concept of a four-sectored machine is shown in Figure 9 which is the most sophisticated cooling design as compared to all other designs. The core idea is creating a return line within the four gaps; in such a way both inlet and outlet would be located on the same side of the machine; as shown in Figure 9a. The cooling oil enters from the driving end and passes through the slots made in the stator lamination. Thus, the end windings remain completely submerged in the oil for an effective heat transfer. The cooling oil turns back and takes the passage or gap between the sectors as shown in Figure 9b and Figure 9c. The overall area of the gap between the sectors is significantly higher than that of the cooling slot. Consequently, the coolant return velocity would be lower than that in the lamination slot. This will eventually reduce the convective heat transfer coefficient. Hence, it was decided to restrict the flow by using fins leading to higher flow velocity. Use of fins not only increased the velocity of returning oil, but also increased the area available for the heat transfer. In this design, an equal number of ducts located in the inner and outer diameter of the stator lamination as shown in Figure 9b and Figure 9c were used; the same cross-sectional area was also used in order to achieve an even distribution of the flow. Such configuration was already analysed in detail and experimentally validated in [27]. The same configuration was initially implemented in all designs. Two more improvements were also done; the first consisted into replacing the axial duct along the stator bore with a high conductive ceramic (100 W/m K) in order to create an effective heat path, the second consisted in reducing the number of axial ducts along the stator outer diameter; these two solutions led to reducing the ducts count from 48 to 12. Figure 9b and Figure 9c show the upgrades implemented on the coolant entry.

The thermal analysis was performed in two stages, first a fluid flow analysis only of the stator region was performed to model the fluid flow and estimate the heat transfer coefficients of the wet surfaces, such as windings, lamination and axial ducts; following that the coefficients were used as boundary conditions into the conduction model where the heat transfer and temperature distribution could be observed.

## V. NUMERICAL METHODOLOGY

To accurately capture thermal behavior of the proposed motor, a conjugate heat transfer analysis is carried out. A high-fidelity Computational Fluid Dynamics (CFD) analysis is conducted which is based on finite volume method (FVM). A detailed description of the numerical methodology is presented in the subsequent subsections.

### A. GOVERNING EQUATIONS

The physical problem undertaken in this study required the solution of governing equations (mass, momentum, and

TABLE 5. Thermophysical properties of solid materials considered.

Components	Density, $\rho$ (kg/m <sup>3</sup> )	Thermal Conductivity, $k_{th}$ (W/m/°C)	Specific Heat (kJ/kg/°C)
Winding	8933	401	0.385
Stator Lamination	7490	30	0.45
Insulation	1400	0.2	1.7
Casing	2790	168	0.833

TABLE 6. Thermophysical properties of cooling oil considered.

Temperature (°C)	Density, $\rho$ (kg/m <sup>3</sup> )	Thermal Conductivity, $k_{th}$ (W/m/°C)	Specific Heat (kJ/kg/°C)	Viscosity $\mu$ (kg/ms)
50	975.8	0.149	1.905	0.021468
100	939.4	0.144	2.01	0.004697
150	905.8	0.14	2.15	0.002083
200	872.2	0.133	2.303	0.001134

TABLE 7. Parameters of experimental machine.

PARAMETERS	VALUE	UNIT
Output Power	20	kW
Base Speed	12,400	rpm
Maximum Speed	14,200	rpm
DC-Link Voltage per Channel	540	V
Outer Diameter	160	mm
Stack Length	30	Mm
Cooling Arrangement	Slot Cooling	-
Rotor Cooling	Dry	-
Winding Heat Generation	7.7	MW/m <sup>3</sup>
Lamination Heat Generation	1.98	MW/m <sup>3</sup>
Coolant Inlet Temp	30	°C
Coolant Flow Rate	5	l/min

energy). These governing equations are described in Eq. (1)-(3). Fluid flow is assumed to be incompressible and turbulent based on the Reynolds number in the present study.

$$\frac{\partial \bar{u}_i}{\partial x_i} = 0 \tag{1}$$

$$\rho \left[ \frac{\partial \bar{u}_i}{\partial t} + \bar{u}_j \frac{\partial \bar{u}_i}{\partial x_j} \right] = -\frac{\partial \bar{u}}{\partial x_i} + \frac{\partial}{\partial x_j} \left[ \mu \left( \frac{\partial \bar{u}_i}{\partial x_j} + \frac{\partial \bar{u}_j}{\partial x_i} - \overline{\rho u'_i u'_j} \right) \right] \tag{2}$$

$$\rho \left[ \frac{\partial \bar{u}}{\partial t} + \bar{u}_j \frac{\partial \bar{u}}{\partial x_j} \right] = \frac{\partial}{\partial x_j} \left[ \frac{\mu}{Pr} \left( \frac{\partial \bar{u}}{\partial x_j} - \overline{\rho T' u'_j} \right) \right] \tag{3}$$

A two-equation, eddy-viscosity based Reynolds Averaged Navier-Stokes (RANS) model (realizable k- $\epsilon$ ) is used in the present study following Singh et al. cite29,30,31. Some of the terms in the governing equation change and some are added as a result of the Reynolds averaging process. The Reynolds averaged velocity, pressure, and temperature are represented by  $\bar{u}_i$ ,  $\bar{u}$ , and  $\bar{u}$  in Eq. (2)-(4), whilst the variations to the corresponding values are denoted by  $u_i'$  and  $T'$ . The additional terms in the governing equations such turbulent shear stress  $-\overline{\rho u'_i u'_j}$  is modeled as (4):

$$-\overline{u'_i u'_j} = \nu_t \left( \frac{\partial \bar{u}_i}{\partial x_j} + \frac{\partial \bar{u}_j}{\partial x_i} - \frac{2}{3} k \delta_{ij} \right) \tag{4}$$

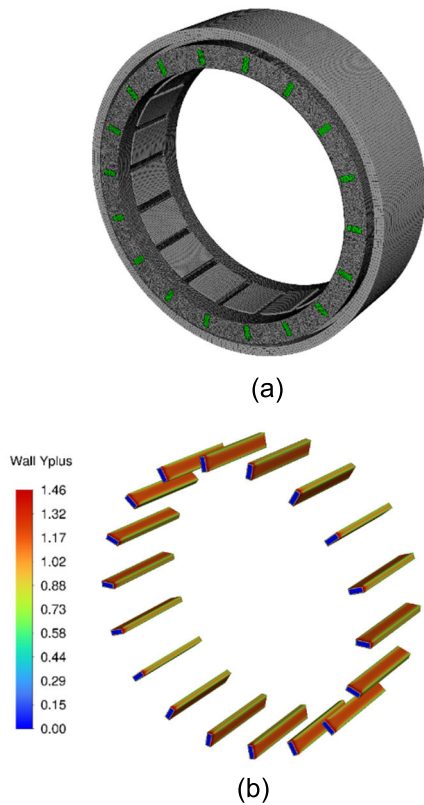


FIGURE 11. (a) Typical mesh used in the present study (b) Wall Y+ contours on the channel walls.

where  $v_t$  is the additional turbulent viscosity. In this work, the turbulent viscosity and other turbulence parameters such as turbulent kinetic energy TKE ( $k$ ), and turbulent energy dissipation ( $\epsilon$ ) are modelled using realizable  $k-\epsilon$  model.

$$\rho \bar{u}_j \frac{\partial k}{\partial x_j} = \frac{\partial}{\partial x_j} \left[ \left( \mu + \frac{\mu_t}{\sigma_k} \right) \frac{\partial k}{\partial x_j} \right] + G_k + G_b - \rho \epsilon + S_k \quad (5)$$

$$\rho \bar{u}_j \frac{\partial \epsilon}{\partial x_j} = \frac{\partial}{\partial x_j} \left[ \left( \mu + \frac{\mu_t}{\sigma_\epsilon} \right) \frac{\partial \epsilon}{\partial x_j} \right] + \rho C_1 S \epsilon - \rho C_2 \frac{\epsilon^2}{k + \sqrt{\nu \epsilon}} + C_{1\epsilon} \frac{\epsilon}{k} C_{3\epsilon} G_b + S_\epsilon \quad (6)$$

Equation (5)-(6) denotes the generation of TKE due to mean velocity gradients ( $G_k$ ), buoyancy ( $G_b$ ), the turbulent Prandtl numbers ( $\sigma_k$  and  $\sigma_\epsilon$ ), constants ( $C_2$  and  $C_{1\epsilon}$ ), and source terms ( $S_k$  and  $S_\epsilon$ ) to the TKE and dissipation equations, respectively.  $C_1$  is a function of the mean strain rate tensor  $S$ . Further, the turbulent viscosity discussed earlier is calculated as:

$$v_t = C_\mu \frac{k^2}{\epsilon} \quad (7)$$

where,  $C_\mu$  is again the function of TKE, turbulence dissipation rate, mean strain rate tensor, and mean rotation rate tensor.

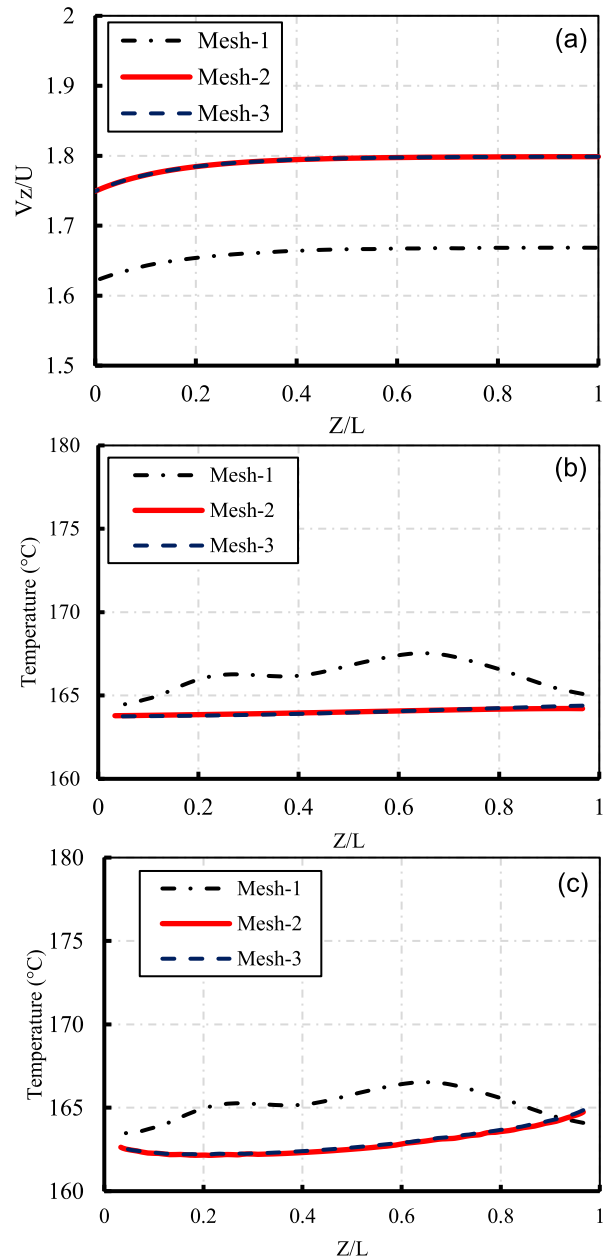


FIGURE 12. Variation of (a) non-dimensional axial velocity (b) lamination temperature (c) winding temperature for the investigated grids.

TABLE 8. Numerically estimated heat transfer coefficients.

Surface	Heat Transfer Coefficient $h$ (W/m <sup>2</sup> K)
Axial ducts	3,800
End-windings (inlet side)	2,260
End-windings (outlet side)	1,530
Lamination wet wall (inlet side)	2,460
Lamination wet wall (outlet side)	990

### B. MATERIAL PROPERTIES

The thermophysical properties of the material considered in this study are listed in Table 5 and Table 6 for solid and fluid

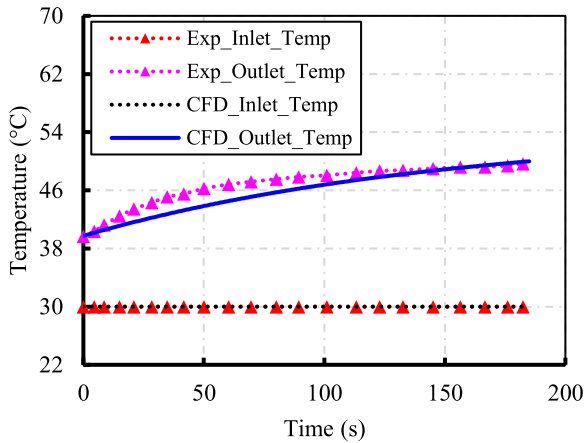


FIGURE 13. Validation of numerical methodology with in-house experimental results.

TABLE 9. Comparison of estimated temperatures for 50 kW output.

Component	Benchmark Machine	Two-sector design	Four-sector design
Stator Iron (max)	100	109	116
Windings (max)	119	133	138
Windings (avg.)	107	112	119

respectively. Generally, insulation thickness on the copper winding is of the order of micron. Instead of modelling insulation material, an equivalent thermal conductivity approach is used to reduce the computational cost. Thermal conductivities were assigned along the three spatial dimensions, more specifically 0.5 and 180 W/m K were assigned along the direction perpendicular to the conductors

and parallel to the conductors respectively; this allowed taking into account the multi-material composition of the stator slots. The temperature dependent fluid properties are considered for the working fluid i.e., JetA1.

C. BOUNDARY CONDITIONS

The computational domain considered in the present study includes oil flow from the inlet to the outlet. The fluid flow analysis was carried out assuming JetA1 as primary coolant and a flow rate of 15 l/min at an initial temperature of 80°C; impinging jets were considered at the inlet whilst a single outlet was assumed at the other end of the machine. The copper windings and stator laminations are considered to be source of volumetric heat generation. The losses obtained from the electromagnetic design, in Table 4, are converted into uniform volumetric heat sources and imposed on the respective cell-zones of windings and stator laminations. The turbulent intensity of 5% is specified at the inlet.

D. SOLUTION METHODOLOGY

The Reynolds averaged governing eq. (2)-(4) and turbulent field variable eq. (6)-(7) described earlier are discretized using finite volume method in Ansys Fluent solver. The equations are solved using a fixed value of initial condition and the boundary conditions specified in the boundary

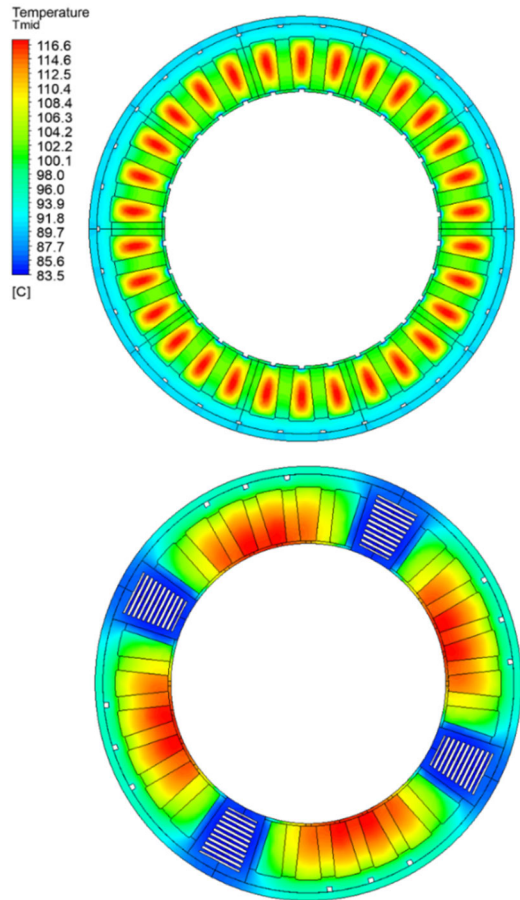


FIGURE 14. Thermal Distribution (a) Existing machine (b) Four sectored machine.

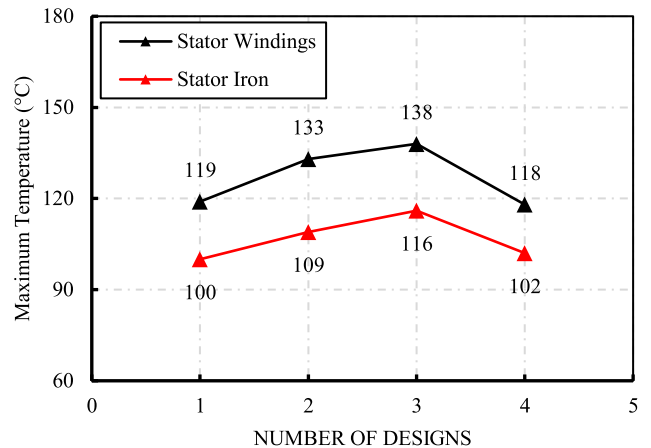


FIGURE 15. Estimated thermal distribution of the benchmark and proposed machine designs (1) Benchmark design (2) Two-sectored design (3) Four-sectored design and (4) Four-sectored design (upgraded).

conditions sub-section. A second-order upwind scheme is used to discretize the convective term of the governing equations and a second order implicit scheme is used for temporal discretization. The SIMPLE algorithm [31] is used for pressure-velocity coupling. The thermophysical properties of the fluid and solid material considered in the present study are described during the solution setup. The convergence criterion is set based on the residuals of the governing equations.

Solution is considered to be converged the residuals of continuity and momentum equations falls below 10<sup>-5</sup> level and for energy residual criterion is set at 10<sup>-8</sup>.

## VI. NUMERICAL METHODOLOGY VALIDATION

In-house experimental motor is used to validate the current numerical methodology. The specifications of the benchmark test motor are given in Table 7. An exploded view of the benchmark motor is shown in Figure 10.

### A. GRID INDEPENDENT STUDY

A grid dependence study is carried out to minimize the errors induced by the grid size in the numerical analysis. Three difference grids with mesh size of 1.65 million (Mesh1), 3.2 million (Mesh2), and 6 million (Mesh3) are considered for the study. A typical mesh used in this study is shown in Figure 11a. Grids are sufficiently resolved in the fluid zone as well as near the contact region to capture sharp gradients in these regions. On the fluid flow side, first cell spacing is kept in such a way that it resolves the buffer zone of the boundary layer i.e., wall Y<sup>+</sup> should be less than 5. It can be noticed from Figure 11b that wall Y<sup>+</sup> is well below 1.5 for all the cooling channels.

Axial velocity of the cooling fluid, winding and lamination temperature are the critical parameters to access grid independence of the solution. The non-dimensional axial velocity along the centerline of the channel is presented in Figure 12a for the investigated grids. It can be observed from this figure that the non-dimensional velocity prediction of Mesh-1 significantly deviated from the Mesh-2 whereas the predictions of Mesh-2 and Mesh-3 are almost identical. The deviation in the predictions of axial velocity of Mesh-1 and Mesh-2 was around 6.67% whereas the same for Mesh-2 and Mesh-3 was less than 0.1%. Similar trends were observed for the axial variation of the underpredicted velocity and consequently over-predicted the lamination and winding temperature as can be seen in Figure 12b and Figure 12c. The difference in the predictions of Mesh-2 and Mesh-3 is around 0.1%. Because Mesh-2 is more computationally efficient and equally accurate than Mesh-3, therefore, it is chosen for further investigation.

### B. EXPERIMENTAL VALIDATION

After selecting the mesh that gave grid independent solution, the predictions of the selected mesh were compared with the benchmark experimental results. In the experimental study, inlet and outlet temperature of the working fluid was measured. The numerical predictions are compared with the experimental results and presented in Figure 13. It can be noticed that the initially when motor is started ( $t < 90$ s), numerical results underpredicted the oil outlet temperature by 2-3°C. It may be due to residual heat in the experimental motor (windings and lamination) due to repeated experiments whereas numerical simulations assumed ambient conditions at the beginning of the test. The settling temperature predicted by numerical simulations is in consensus with the

experimental measurements. Hence, numerical methodology adopted in the present study can be relied upon.

## VII. THERMAL RESULTS & DISCUSSION

The validated numerical model is implemented to predict thermal performance of the baseline and four-sectored machine. Due to the negligible power loss in the rotor only the stationary components were modelled to reduce the computational cost similar to the validation test case. As mentioned earlier, the thermal analysis was performed in two stages. In the first stage a fluid flow analysis only of the stator region was performed to model the fluid flow and estimate the heat transfer coefficients of the wet surfaces, such as windings, lamination and axial ducts. Table 8 shows the heat transfer coefficients estimated, as it can be noted higher heat transfer coefficients were predicted at the inlet side, this was caused by the higher turbulence induced by the impinging jets. Another reason of getting higher heat transfer at the inlet size is the temperature difference between the cooling oil at the inlet and outlet. The cooling oil got heated as it moves from inlet to outlet side. Consequently, a lower temperature gradient between the cooling oil and the hot surface is available at the outlet side as compared to the inlet side.

Local numerical fluid flow and heat transfer analyses of the finned ducts were carried out to identify the most appropriate spacing and to estimate the heat transfer coefficient achievable. An optimal spacing of 1 mm was identified, leading to an increase of the surface of heat transfer and of the convective heat transfer coefficient both by five times compared to the case without fins.

In the second stage of thermal analysis, the heat transfer coefficients were used as boundary conditions into the conduction model where the heat transfer and temperature distribution could be observed. Based on the electromagnetic design the following power losses, in Table 4, were assumed and implemented as volumetric heat generation. By implementing the above data into the conduction model, the temperature distribution within the machine could be then predicted, the results of which are shown in Table 9.

Figure 14 shows the comparison between the temperature distribution in the existing machine and in the four-sector machine. As can be noted a considerable temperature reduction was achieved; indeed, such improved design led the winding maximum and average temperatures to be one and two degrees lower compared to the benchmark machine despite the higher power loss density. Figure 15 also summarizes the key maximum temperatures of windings and iron in all the machine designs considered in this study. This further highlights the benefits obtained from the improved cooling design. The temperature of both the winding and the stator iron of four sectored design is comparable with that of the baseline design despite of increased loss density.

## VIII. CONCLUSION

This paper proposed novel sectored dual three-phase PM machines designed to meet fault-tolerant requirements, which

are essential during the design phase in safety-critical applications such as aerospace and marine industries. This was achieved by removing a pole-pair section from the stator while leaving the rotor unchanged, resulting in air sectors within the motor's stator. An in-depth performance analysis of the proposed machines was conducted and compared with the benchmark machine design for a given output power of 50 kW. The following conclusions can be drawn from the present work:

- The results have shown that the proposed four-sectored PM machine met all the fault-tolerant requirements in terms of magnetic, physical, and thermal isolation between the two three-phase channels, unlike the benchmark machine.
- However, this advantage comes at the expense of a 5.2% torque ripple, which is 3.2% higher than that observed in the benchmark machine design.
- Additionally, peak temperature in the novel designed was increased due to increased power density.
- In order to maintain the identical or better thermal performance compared to the baseline design, an efficient cooling system was successfully implemented.
- In this design, the gaps between the sectors were utilized as flow paths for the cooling medium.
- An array of fins was added to the stator laminations in the gaps made due to sectoring. The radial spacing between the fins were optimized and found to be 1mm for the design considered.
- The optimized finned channels did not only increase the surface available by five times, but it also increases the convective heat transfer coefficient by the same quantity, thanks to the higher turbulence level achieved.
- Ceramic inserts were also used at the top of the stator tooth slot opening to boost the conductive heat transfer from the active coils. Such arrangement allowed to achieve an equal temperature distribution compared to the original design, despite the 20% higher power losses.
- The upgraded cooling arrangement has also led to a temperature reduction of approximately 15% in comparison to the initial cooling system used in the four-sector machine.
- Overall, an increase of current density of 18.2% was achieved, representing an increase of  $2A/mm^2$  with respect to benchmark design.

## REFERENCES

- [1] G. Sala, D. Gerada, C. Gerada, and A. Tani, "Radial force control for triple three-phase sectored SPM machines. Part I: Machine model," in *Proc. IEEE Workshop Electr. Mach. Design, Control Diagnosis (WEMDCD)*, Apr. 2017, pp. 193–198, doi: [10.1109/WEMDCD.2017.7947746](https://doi.org/10.1109/WEMDCD.2017.7947746).
- [2] M. Barcaro, N. Bianchi, and F. Magnussen, "Faulty operations of a PM fractional-slot machine with a dual three-phase winding," *IEEE Trans. Ind. Electron.*, vol. 58, no. 9, pp. 3825–3832, Sep. 2011, doi: [10.1109/TIE.2010.2087300](https://doi.org/10.1109/TIE.2010.2087300).
- [3] N. Bianchi and M. Dai Pre, "Use of the star of slots in designing fractional-slot single-layer synchronous motors," *IEE Proc. - Electric Power Appl.*, vol. 153, no. 3, p. 459, 2006, doi: [10.1049/ip-epa:20050284](https://doi.org/10.1049/ip-epa:20050284).
- [4] A. Tani, G. Serra, M. Mengoni, L. Zarri, G. Rini, and D. Casadei, "Dynamic stator current sharing in quadruple three-phase induction motor drives," in *Proc. IECON 39th Annu. Conf. IEEE Ind. Electron. Soc.*, Nov. 2013, pp. 5173–5178, doi: [10.1109/IECON.2013.6699975](https://doi.org/10.1109/IECON.2013.6699975).
- [5] M. Rottach, C. Gerada, T. Hamiti, and P. W. Wheeler, "Fault-tolerant electrical machine design within a rotorcraft actuation drive system optimisation," in *Proc. 6th IET Int. Conf. Power Electron., Mach. Drives (PEMD)*, Mar. 2012, pp. 1–6, doi: [10.1049/cp.2012.0247](https://doi.org/10.1049/cp.2012.0247).
- [6] V. Madonna, P. Giangrande, C. Gerada, and M. Galea, "Thermal analysis of fault-tolerant electrical machines for aerospace actuators," *IET Electr. Power Appl.*, vol. 13, no. 7, pp. 843–852, Jul. 2019.
- [7] R. Lehmann, A. Petuchow, M. Moullion, M. Künzler, C. Windel, and F. Gauterin, "Fluid choice based on thermal model and performance testing for direct cooled electric drive," *Energies*, vol. 13, no. 22, p. 5867, Nov. 2020.
- [8] P. S. Ghahfarokhi, A. Podgornovs, A. Kallaste, A. J. M. Cardoso, A. Belahcen, and T. Vaimann, "The oil spray cooling system of automotive traction motors: The state of the art," *IEEE Trans. Transport. Electrific.*, vol. 9, no. 1, pp. 428–451, Mar. 2023.
- [9] K. S. Garud, S.-G. Hwang, J.-W. Han, and M.-Y. Lee, "Performance characteristics of the direct spray oil cooling system for a driving motor of an electric vehicle," *Int. J. Heat Mass Transf.*, vol. 196, Nov. 2022, Art. no. 123228.
- [10] A. Saleem, M. H. Park, T. Ambreen, and S. C. Kim, "Optimization of oil flow distribution inside the in-wheel motor assembly of electric vehicles for improved thermal performance," *Appl. Thermal Eng.*, vol. 201, Jan. 2022, Art. no. 117753.
- [11] Z. Xu, A. L. Rocca, P. Arumugam, S. J. Pickering, C. Gerada, S. Bozhko, D. Gerada, and H. Zhang, "A semi-flooded cooling for a high speed machine: Concept, design and practice of an oil sleeve," in *Proc. IECON 43rd Annu. Conf. IEEE Ind. Electron. Soc.*, Oct. 2017, pp. 8557–8562.
- [12] F. Zhang, D. Gerada, Z. Xu, C. Liu, H. Zhang, T. Zou, Y. C. Chong, and C. Gerada, "A thermal modeling approach and experimental validation for an oil spray-cooled hairpin winding machine," *IEEE Trans. Transport. Electrific.*, vol. 7, no. 4, pp. 2914–2926, Dec. 2021.
- [13] B. Bickel, J. Franke, and T. Albrecht, "Manufacturing cell for winding and assembling a segmented stator of PM-synchronous machines for hybrid vehicles," in *Proc. 2nd Int. Electr. Drives Prod. Conf. (EDPC)*, Oct. 2012, pp. 1–5, doi: [10.1109/EDPC.2012.6425109](https://doi.org/10.1109/EDPC.2012.6425109).
- [14] J. Bretschneider, R. Spitzner, and R. Boehm, "Flexible mass production concept for segmented BLDC stators," in *Proc. 3rd Int. Electr. Drives Prod. Conf. (EDPC)*, Oct. 2013, pp. 1–8, doi: [10.1109/EDPC.2013.6689734](https://doi.org/10.1109/EDPC.2013.6689734).
- [15] G. J. Li, Z. Q. Zhu, W. Q. Chu, M. P. Foster, and D. A. Stone, "Influence of flux gaps on electromagnetic performance of novel modular PM machines," *IEEE Trans. Energy Convers.*, vol. 29, no. 3, pp. 716–726, Sep. 2014, doi: [10.1109/TEC.2014.2312429](https://doi.org/10.1109/TEC.2014.2312429).
- [16] N. S. Lobo, E. Swint, and R. Krishnan, "M-phase N-segment flux-reversal-free stator switched reluctance machines," in *Proc. IEEE Ind. Appl. Soc. Annu. Meeting*, Oct. 2008, pp. 1–8, doi: [10.1109/08ias.2008.69](https://doi.org/10.1109/08ias.2008.69).
- [17] V. Madonna, P. Giangrande, C. Gerada, and M. Galea, "Thermal analysis of fault-tolerant electrical machines for more electric aircraft applications," *J. Eng.*, vol. 2018, no. 13, pp. 461–467, Jan. 2018, doi: [10.1049/joe.2018.0040](https://doi.org/10.1049/joe.2018.0040).
- [18] T. V. T. Nguyen, N.-T. Huynh, N.-C. Vu, V. N. D. Kieu, and S.-C. Huang, "Optimizing compliant gripper mechanism design by employing an effective bi-algorithm: Fuzzy logic and ANFIS," *Microsyst. Technol.*, vol. 27, no. 9, pp. 3389–3412, Sep. 2021.
- [19] M. Polikarpova, "Liquid cooling solutions for rotating permanent magnet synchronous machines," Ph.D. dissertation, Dept. Energy Technol., LUT School Technol., Lappeenranta Univ. Technol., Lappeenranta, Finland, 2014.
- [20] D. H. Lim and S. C. Kim, "Thermal performance of oil spray cooling system for in-wheel motor in electric vehicles," *Appl. Thermal Eng.*, vol. 63, no. 2, pp. 577–587, Feb. 2014.
- [21] F. R. Ismagilov, V. E. Vavilov, and D. V. Gusakov, "Design features of liquid-cooled aviation starter generators," in *Proc. IEEE Int. Conf. Electr. Syst. Aircr., Railway, Ship Propuls. Road Vehicles Int. Transp. Electrific. Conf. (ESARS-ITEC)*, Nov. 2018, pp. 1–5.
- [22] Z. Huang, S. Nategh, V. Lassila, M. Alaküla, and J. Yuan, "Direct oil cooling of traction motors in hybrid drives," in *Proc. IEEE Int. Electr. Vehicle Conf.*, Mar. 2012, pp. 1–8.

- [23] C. Dong, Y. Qian, Y. Zhang, and W. Zhuge, "A review of thermal designs for improving power density in electrical machines," *IEEE Trans. Transport. Electric.*, vol. 6, no. 4, pp. 1386–1400, Dec. 2020.
- [24] Y. Gai, M. Kimiabeigi, Y. Chuan Chong, J. D. Widmer, X. Deng, M. Popescu, J. Goss, D. A. Staton, and A. Steven, "Cooling of automotive traction motors: Schemes, examples, and computation methods," *IEEE Trans. Ind. Electron.*, vol. 66, no. 3, pp. 1681–1692, Mar. 2019.
- [25] H. Kellermann, A. L. Habermann, P. C. Vratny, and M. Hornung, "Assessment of fuel as alternative heat sink for future aircraft," *Appl. Thermal Eng.*, vol. 170, Apr. 2020, Art. no. 114985.
- [26] C. Liu, Z. Xu, D. Gerada, J. Li, C. Gerada, Y. C. Chong, M. Popescu, J. Goss, D. Staton, and H. Zhang, "Experimental investigation on oil spray cooling with hairpin windings," *IEEE Trans. Ind. Electron.*, vol. 67, no. 9, pp. 7343–7353, Sep. 2020.
- [27] A. L. Rocca, "Thermal analysis of a high speed electrical machine," Ph.D. dissertation, Dept. Mech., Mater., Manuf. Eng., Univ. Nottingham, Nottingham, U.K., 2016.
- [28] K. Singh and Udayraj, "Combined film and impingement cooling of flat plate with reverse cooling hole," *Appl. Thermal Eng.*, vol. 208, May 2022, Art. no. 118224.
- [29] A. Yousefi, A. Nejat, and M. H. Sabour, "Ribbed channel heat transfer enhancement of an internally cooled turbine vane using cooling conjugate heat transfer simulation," *Thermal Sci. Eng. Prog.*, vol. 19, Oct. 2020, Art. no. 100641.
- [30] A. M. Divakaran, E. Gkanas, J. Jewkes, S. Shepherd, W. Jamal, S. Faramehr, and E. Abo-Serie, "Experimental investigation and 3D CFD based numerical evaluation of conjugate heat transfer in wheel hub motors used in micro-mobility vehicles," [Online]. Available: <https://ssrn.com/abstract=4805523>
- [31] S. Patankar, *Numerical Heat Transfer and Fluid Flow*. Boca Raton, FL, USA: CRC Press, 2018.



**MUHAMMAD RAZA KHOWJA** received the B.Eng. degree (Hons.) in electrical power engineering from the Mehran University of Engineering & Technology, Jamshoro, Pakistan, in 2011, the M.Sc. degree in electrical engineering, in 2012, and the Ph.D. degree in electrical and electronics engineering from the University of Nottingham, U.K., in 2018. He is currently a Research Fellow with the Power Electronics, Machines, and Control (PEMC) Group, University of Nottingham. His main research interests include integrated passive components, the design and development of high-performance electrical machines for aerospace applications, and the characterization of insulating materials for electrical machine applications.



**KULDEEP SINGH** received the Ph.D. degree in the design of the cooling configuration of an aero-engine afterburner from the Mechanical Engineering Department, Indian Institute of Technology Delhi, New Delhi, India, in 2016. He subsequently worked as a Senior Research Fellow with Rolls Royce UTC, Gas Turbine and Transmission Research Centre, University of Nottingham, Nottingham, U.K. He is currently a Senior Applications Engineer with NDSS-DER, University of Nottingham. His main research interests include the design of efficient cooling systems for high-performance, power-dense electrical machines for aerospace and automotive applications, multiphase flows, computational fluid dynamics, and machine learning augmented numerical analysis.



**ANTONINO LA ROCCA** received the Ph.D. degree from the Department of Mechanical, Materials, and Manufacturing Engineering, University of Nottingham, U.K., in 2016. He is currently a Research Fellow with the Fluids and Thermal Engineering Research Group and the Power Electronics, Machines and Control Research Group, Faculty of Engineering, University of Nottingham. His research interests include the thermo-mechanical modeling and design of high-speed and high-power dense electrical machines, power electronics and battery packs for advanced generation and propulsion systems by the use of lumped parameters thermal networks (LPTN) and computational fluid dynamics (CFD), and FEA.



**GAURANG VAKIL** (Member, IEEE) received the Ph.D. degree in variable speed generator design for renewable energy applications from the Power Electronics, Machines and Drives Group, Indian Institute of Technology Delhi, New Delhi, India, in 2016. He subsequently worked as a Research Associate with the Power Electronics, Machines and Controls Group, University of Nottingham, Nottingham, U.K. In 2016, he was appointed as an Assistant Professor with the Electrical and Electronics Engineering Department, University of Nottingham. His main research interests include design and development of high-performance electrical machines for transport and propulsion, optimizing electric drive-train for pure electric and hybrid vehicles (aerospace and automotive), high power density machines, and magnetic material characterization.



**RAMKUMAR RAMNATHAN** received the B.Tech. degree in electrical engineering from Anna University, India, in 2014. He is currently pursuing the dual M.Tech. and Ph.D. degree from Indian Institute of Technology Bombay, Mumbai, India. He is currently a Research Associate with the University of Nottingham, U.K. His research interests include the design of high-speed motors for electric vehicles and aerospace applications, and the characterization, and modeling of advanced magnetic materials.



**CHRIS GERADA** (Member, IEEE) received the Ph.D. degree in numerical modeling of electrical machines from the University of Nottingham, Nottingham, U.K., in 2005. He subsequently worked as a Researcher with the University of Nottingham on high-performance electrical drives and the design and modeling of electromagnetic actuators for aerospace applications. Since 2006, he has been the Project Manager of GE Aviation Strategic Partnership. In 2008, he was appointed as a Lecturer in electrical machines, 2011, an Associate Professor, and a Professor with the University of Nottingham, in 2013. His main research interests include the design and modeling of high-performance electric drives and machines. He is currently the past Chair of the IEEE IES Electrical Machines Committee. He is an Associate Editor of IEEE TRANSACTIONS ON INDUSTRY APPLICATIONS.

...